Metal catalysts supported on biochars: Part I Synthesis and characterization

Jose Luis Santos[a,], Päivi Mäki-Arvela[b], Antonio Monzón[c], Dmitry Yu Murzin[b] and Miguel Ángel Centeno[a]*

[a] *Instituto de Ciencia de Materiales de Sevilla, Centro Mixto CSIC-Universidad de Sevilla, 41092 Sevilla, Spain*

[b] *Johan Gadolin Process Chemistry Centre, Åbo Akademi University, FI-20500 Turku, Finland*

[c] *Instituto de Nanociencia de Aragón (INA) e Instituto de Ciencia de Materiales de Aragón (ICMA), Universidad de Zaragoza-CSIC, 50018 Zaragoza, Spain*

**corresponding author: josel.santos@icmse.csic.es*

ABSTRACT

In the current study, synthesis and detailed characterization of cellulose biochars as a waste biomass model component and vine shoot biochars as a real waste biomass catalyst was performed. Although initially biochars exhibit poor textural properties, a simple activation process can make them much more suitable as a catalyst supports. A combination of physical (CO_2) and chemical activation ($ZnCl_2$) was evaluated. The characterization results indicated that the surface area and pore volume of the biochars have increased significantly by chemical activation treatment with $ZnCl_2$. A series of metal catalysts (Pd, Au and Ru) supported on biochars was prepared and characterized. The prepared materials represent a set of noble metal catalysts supported on biochars with different textural and surface properties, which can be used to evaluate the catalytic role of the active phase and carbon support nature in catalytic reactions of interest, such as hydrodeoxygenation, described in the part II.

Keywords: Biochars, Pd, Au, Ru supported, synthesis and characterization, Hydrodeoxygenation.

1. Introduction

As the most abundant and renewable resource in the world, biomass is widely considered as an auspicious alternative to fossil sources for providing sustainable fuels and chemicals. [1] For decades, upgrading biomass into fuels, fine chemicals, and materials has attracted worldwide attention. In the process of energy production from biomass, biochars are a residual byproducts of thermochemical degradation [2]. Mostly, biomass is a lignocellulosic structure, constituted by cellulose (38-50%), hemicelluloses (23-32%), lignin (15-25%) and small amounts of extractives [3]. In fact, produced biomaterials from commercial cellulose can be a good approximation towards the further use of real biomass wastes and has been extensively studied [4-6]. While numerous studies about different kinds of biomass wastes have been reported previously; including hardwood [7], peanut hull [8], rice husk [9] or corn stover [10] the use of vine shoot as a raw material for biochar generation has not been reported extensively before [11-13]. Producing biochar from vine shoots, a residual lignocellulosic biomass from vine pruning, is an interesting pathway to manage this waste and simultaneously generate environmental and agronomic benefits. Moreover, as compared to some other carbonaceous materials, biochars are less expensive and can be used for many purpose [14,15]. Direct utilization, without any treatment, of these biochars is however not straight forward because of their poor textural and psychochemical properties. In order to improve the textural properties of the resulting biochars, various activation approaches, both physical and chemical ones have been investigated [16]. As already suggested by Lopez-Gonzalez et al. [17] a combination of both activation procedures is possible for the generation of biochars with very large surface areas as well as highly developed meso and macroporosity. However, according to our knowledge, this double activation process, both physical and chemical, has not been reported so far for biochars coming from vine

shoots. More importantly, this combined into one stage procedure of activation in a single stage, leads to formation of stronger activated biochars with a great potential to be used as versatile catalytic supports in many chemical processes [18,19].

The utilization of different sources of biomass for formation of biocarbons is being recently a subject of many studies [20,21] after demonstration their applicability as catalysts in biodiesel production.

In general, carbonaceous materials exhibit interesting properties allowing their use as heterogeneous catalysts. In particular, they have been described as optimal one for reactions relevant to biomass valorization [22-24]. Besides low costs, stability, reusability and easiness of regeneration [25] the surface and textural properties can be tailored. The use of noble metals as an active phase (Pd [26], Pt [27], Ru [28] and Au [29]) has been extensively reported previously. Although noble metals are generally more expensive than non-noble ones, their use at low loadings is often done, for instance in oil refining processes, such as hydrocracking, catalytic reforming or isomerization and in production of bulk and specialty chemicals. Superior catalytic performance of noble metals and available technologies for spent catalysts recycling justify their application in different industrial catalytic processes despite higher costs compared to non-precious metals. Synthesis of nanosized metal particles supported on biochars is typically performed with wetness impregnation [30,31]. However, high costs of these catalysts makes it necessary to optimize the product yield and to maximize the dispersion of the metal component the latter is needed since the rates of catalytic reaction are, in general, proportional to the number of available surface metal atoms. Specifically, hydrodeoxygenation of phenolic lignin derived compounds studied in this work requires high metal dispersion [32].

Due to difficulties of synthesizing small gold nanoparticles using hydrophobic supports such biochars by conventional impregnation methods, other deposition techniques have

been developed for the gold nanoparticles preparation. A colloidal method is considered as the most appropriate to obtain a homogeneous and reproducible gold nanoparticles size distribution allowing a more direct correlation bet size of gold size and reactivity [33,34]. The colloidal method for preparing Au/C catalyst includes utilization of such particle stabilizing agents as citrates, polyvinyl alcohol (PVA) etc., which thereafter must be mildly reduced using for example chemical reduction agents.

The aim in this work was to synthesize different metal nanoparticles (Ru, Pd, Au) supported on biochar of different textural properties and nature. Such approach allows elucidation of potential synergy between the noble metals, and optimized textural properties of the starting biochars. Generation of micro and mesoporous catalysts with a defined pore distribution and appropriate metal dispersion on the biochar surface can lead to efficient catalysts for biomass valorization. The catalysts were exhaustively and comprehensively characterized by elemental analysis, X-ray diffraction (XRD), diffuse reflectance infrared fourier transform spectroscopy (DRIFTS), nitrogen physisorption, high resolution transmission electron microscopy (HR-TEM), high resolution scanning electron microscopy (HR-STEM), scanning electron microscopy (SEM), inductively coupled plasma (ICP), energy dispersive X-ray spectroscopy (EDX) mapping, zeta potential measurements and pH determination of the catalyst slurries. These catalysts were eventually tested in vanillin hydrodeoxygenation as described in the accompanying paper.

2. Experimental

1.1. Catalysts preparation

Raw commercial microcrystalline cellulose (Sigma-Aldrich, 100 mesh particle size) was used as a model of cellulosic biomass, and vine shoot (crushed, particle diameter below

1 mm, from Viñas del Vero SA winery, Barbastro (Huesca, Spain)), as a model of residual biomass.

Due to the natural origin of the residual biomass used, the percentage of the mineral load in the resulting biochar could be very high and difficult to be controlled, preventing its reproducibility [11]. Therefore, to facilitate reproducibility, a demineralization method of the residual biomass was used. In particular, crushed vine shoot was treated with nitric acid (HNO_3, 50% vol.) at room temperature for half an hour in order to remove most of the mineral load. After that, the vine shoot was washed with distilled water until neutral pH. The biochars were obtained by slow pyrolysis of both materials (microcrystalline cellulose and treated vine shoot) in a horizontal tubular oven under the following conditions: final temperature of 800 °C with a heating rate of 10 °C·min^{-1}, in CO_2 atmosphere of 200 mL·min^{-1} of total flow. The solid was cooled down in an inert atmosphere (N_2, 200 mL·min^{-1}). The generated solids are named as C_{cel} CO_2 and C_{vin} CO_2, depending on the raw material used for pyrolysis.

Since catalytic activity is strongly dependent on accessibility of the reactants to the active sites distributed across the porous structure of the solids [35], it is very interesting to increase the porosity of the biochars, mostly the pores diameter, by generation of mesoporosity. Chemical activation is a well-known technique for the preparation of mesoporous carbons. It has some intrinsic advantages over physical activation by carbon gasification: it proceeds at lower temperatures and is carried out in a single step typically producing higher yields and very high specific surface areas. For that purpose, several chemical pretreatments (KOH, H_3PO_4, $ZnCl_2$, etc…) were proposed in the literature [12, 36, 37].

In our case, it was decided to treat both raw materials by impregnating them with 500 mL of an aqueous solution of $ZnCl_2$ (2:1 weight ratio of $ZnCl_2$: biomass), followed by heating

until complete evaporation of the remaining solution (complete dryness). Thereafter, the dry material was submitted to the same slow pyrolysis procedure as described above. In this way, a double activation process, both physical and chemical, is carried out. It must be mentioned that $ZnCl_2$ leftovers can remain on the carbonaceous materials produced. In order to remove these residues, a washing procedure, first with an aqueous solution of hydrochloric acid (HCl 0,5% vol.) and then with distillated water until neutral pH, was applied. The generated solids were coded as C_{cel} $ZnCl_2$ CO_2 and C_{vin} $ZnCl_2$ CO_2.

Due to the hydrophobic character of the biochar, Ru and Pd catalysts were prepared by wetness impregnation with acetone solutions of ruthenium (III) nitrosyl nitrate (Johnson Matthey; purity = 14.34%) and palladium (II) acetate (Johnson Matthey; purity = 47.14%), respectively. In all cases, the catalysts were synthetized with a nominal value of 2% (wt.%) of the metal. 2 g of the dried carbon support were deposited in a mortar. After that, required amounts of $1x10^{-3}$ M solution of the corresponding metallic precursor in acetone were added dropwise. Then, the solids were dried at 100 °C for 2 h and finally reduced at 300 °C for 2 h in a 300 mL/min nitrogen/hydrogen (1:1) flow.

Gold catalysts were prepared by colloidal synthesis, due to the well-known difficulty of obtaining small gold particle sizes by wetness impregnation [38]. Chloroauric (II) acid, $HAuCl_4$ (Johnson Matthey, purity = 49.81%) was used as a precursor. The gold deposition was carried out according to the colloidal method assisted by polyvinyl alcohol (PVA) using $NaBH_4$ as reducing agent [39]. The conditions were previously optimized in a previous work [34]. The necessary amount of the gold precursor was dissolved in distilled water to the final concentration of $5 \cdot 10^{-4}$M. Thereafter, an adequate quantity of PVA (1% wt. aqueous solution, 1:5 Au/PVA weight ratio) was added followed by stirring for 20 min. After that, the appropriate amount of freshly prepared 0.1 M $NaBH_4$ solution was quickly added to reduce the gold precursor. After 20 min stirring, the solution was put in

contact with the pre-determined amount of the biochar support in order to have a nominal gold loading of 2%wt. After 45 min the final mixture was centrifuged at 15000 rpm for 20 min in order to ensure anchoring of gold nanoparticles on charcoal. The resulted samples were filtered and dried at 100 °C for 2 h and finally calcined at 300 °C for 2 h in static air in order to remove the leftovers of PVA from the surface of the gold nanoparticles.

The obtained catalysts are named with the nomenclature of the corresponding support preceded by the metal symbol (Pd, Ru and Au).

1.2 Characterization methods

The elemental analysis of the solids was done using a CHNS elementary analyzer (Leco ECO TRUSPEC CHNS MICRO).

Raman spectroscopy measurements were performed on a Horiba Jobin Yvon dispersive microscope (HR800) with a confocal aperture of 1000 microns using a laser spot diameter of 0.72 microns and a spatial resolution of 360 nm. The microscope is equipped with a diffraction grating of 600 grooves/mm, and a CCD detector, using a green laser (λ = 532.14 nm; maximum power 20 mW) and a 50x objective.

XRD measurements were made at room temperature in a X'Pert Pro PANalytical diffractometer with Cu anode, working at 45 kV and 40 mA. Diffractograms were obtained in a continuous scan mode from 10 to 90° 2θ using 0.05° step size and a time per step of 300 seconds. For each diffraction pattern, structural determination was performed by comparison with the database PDF2 ICDD2000 (Powder Diffraction File 2 International Center for Diffraction Data, 2000).

To evaluate the graphitization degree in the samples by XRD, the stacking height parameter (L_c) and the R value (defined graphically according to Li et al. [40]) were determined.

The stacking heights (L_c) were calculated using the empirical Braggs and Scherrer equations [41]:

$$L_c = \frac{Kc \cdot \lambda}{\beta 002 \cdot cos\Theta 002} \quad \textbf{(1)}$$

Where λ is the wavelength of incident X-ray (in our case 1.18 Å for copper K_α radiation); Θ002 is the peak position of (002) band; β002 is the full width at half maximum (FWHM) of the corresponding peak and k_c is a constant depending on X-ray reflection plane (0.89 for the (002) band).

The empirical R-value is defined as the ratio of the (002) peak intensity relative to the background at the same scattering angle. Lower R-values indicate higher concentrations of single layers, with R = 1 indicating no (002) peak in the XRD pattern.

The diffuse reflectance infrared Fourier Transform (DRIFTS) spectra were obtained on a JASCO FTIR 6200 spectrometer with a DRIFTS accessory Pike model EASI-DIFF, at room temperature and accumulating 100 scans with a resolution of 4 cm^{-1}.

Textural properties of the solids were studied from the N_2 physisorption isotherms at 77 K in a Micromeritics Tristar II equipment. Samples were previously degassed at 350 °C for 12 hours using a vacuum degasser system 061 VacPrep of Micromeritics. The BET method was applied for the adsorption isotherms to obtain the specific surface areas. Sizes and pore distribution were calculated from the desorption curve of the isotherm by the BJH method.

Metal content the catalysts was measured by inductively coupled plasma optical emission spectroscopy (ICP-MS) using a Spectro ICP spectrometer (Model: ULTIMA 2).

The average size and size distributions of the metal nanoparticles were measured by high resolution transmission electron microscopy (HR-TEM). HR-TEM micrographs were performed with a FEI Talos electron microscope operated at an acceleration voltage of 200 kV, equipped with a Field Emission filament. Digital images were taken with a side mounted Ceta 16M camera. For HR-TEM preparation, a few milligrams of each sample were deposited directly on 300 mesh holey carbon coated copper TEM-grid. The mean particles sizes were estimated from HR-TEM micrographs by single particle measurements of at least 200 particles.

The mean metal particle diameter was considered on the basis of its homogeneity, dispersion and number of particles. The average particle size was estimated considering the surface distribution calculations:

$$D_p = \frac{\sum n_i d_i^3}{\sum n_i d_i^2} \qquad \textbf{(2)}$$

where d_i is the measured diameter of the i^{th} particle, and n_i the number of particles with this diameter.

Scanning electron micrographs (SEM) were obtained with a scanning electron microscope HITACHI S-4800 FEG-fitted with secondary and electron backscattered detectors and microanalysis energy disperse X-Ray spectroscopy (EDS). SEM micrographs were taken at a working distance of 4 mm and a voltage of 2 kV. Compositional analysis was performed using EDS, at a working distance of 15 mm, and a voltage of 20 kV. Mapping composition was obtained at the same working distance of 15 mm, and a voltage of 5 kV.

The acidity of the solids was evaluated by two different procedures. First, isoelectric Point (IEP) related to bulk acidity, was evaluated by titration, using a pH-electrode (Metrohm) according to the procedure described by Markus et al [42]. Fifty milligrams of the sample were dispersed in fifty milliliters of distilled water, the slurry was continuously stirred by a magnetic stirrer during the measurements, and the pH was measured with time. The isoelectric point of the sample corresponds to that measured when achieving a constant pH value.

The surface acidity was evaluated by measuring the zeta potential with a Malvern Zetasizer Nano-ZS, using 0,1 M HCl solution as an acidity buffer and 0.1 M NaOH as a basicity buffer for the pH adjustment. 20 mg of the sample was dissolved in 10 mL of distilled water under continuous stirring. Measurements were made from pH 2 to pH 11 with an increase of 0.5. Three measurements were obtained for each pH value, being represented the mean one.

2. Results and Discussion

Carbon yields for the prepared biochars were, C_{cel} CO_2 19.8%, C_{vin} CO_2 20.6%, C_{cel} $ZnCl_2$ CO_2 29%; C_{vin} $ZnCl_2$ CO_2 44.8 %. These carbon yields are in good agreement with the values reported previously in the literature [43] for similar biomass waste. In particular, in the case of vine shoot, a carbon yield of 22.9% has been reported after pyrolysis in N_2 atmosphere [11]. The higher carbon yield of C_{vin} compared to C_{cel} is related with the metal content of this waste biomass, around 1% weight (mainly CaO, K_2O, MgO, SiO_2, Fe_2O_3, Al_2O_3 and P_2O_5) [11]. In fact, these elements have been proposed in the literature as catalysts for the cracking of tars [44,45]. For similar considerations, a considerable increase in the carbon yield measured for the $ZnCl_2$-treated biomass is associated, according to Reinoso et al. [9,36], to the lower formation of tars during pyrolysis induced by $ZnCl_2$.

Elemental analysis of carbons and catalysts employed in this work is presented in **Table 1**. All biochars do not contain any sulphur, which is a very attractive characteristic for industrial applications. The carbon content in C_{vin} materials is lower than those of C_{cel} ones, this is related with the mineral content in vine shoot which is not fully removed after the HNO_3 treatment. In a similar way, $ZnCl_2$-treated materials have a lower carbon content that those of the equivalent un-treated biomass, evidencing presence of $ZnCl_2$ leftovers in the carbon after the washing process.

The H/C ratio of a carbon material is indicative of its aromaticity as lower H/C ratio implies higher aromaticity [46]. The H/C values of all carbonaceous materials prepared in this work are very low and characteristic of highly aromatic biochars [47]. Although no significant differences in the H/C ratio are evidenced among the biochars, it can be expected that the treatment with $ZnCl_2$ decreases to a minor extent the biochar aromaticity.

Lower amounts of nitrogen were found in the chars from cellulose. Although this has not been discussed in depth in the literature [11], vine shoot derived biomass, due to their natural character may contain high percentages of nitrogen, because of the nitrogen fixation processes from soils, nitrate fertilizers and other additives used during irrigation and maintenance. This, in addition to the exposure to nitric acid during demineralization, leads to an increase in the percentage of nitrogen in these samples with respect to those generated from cellulose.

On the other hand, as shown in **Table 1**, the wetness impregnation method generates catalysts with the elemental composition of measured elements slightly lower than that of the support, as expected because of metal deposited. In the case of gold catalysts synthetized by the colloidal method, the carbon contents are closer to that of the corresponding support. Carbon and hydrogen content was also similar, indicating an

efficient washing procedure for removal PVA leftovers from the catalyst surface. Obviously, this leads to a closer H/C ratio as in the support for the catalyst prepared by the colloidal route compared to the impregnation one.

Table 1. Elemental Analysis

Sample	*%C*	*%H*	*%N*	*H/C*
$C_{cel}\,CO_2$	93.6	1.1	0.4	0.012
$C_{cel}\,ZnCl_2\,CO_2$	82.9	1.5	1.1	0.018
$C_{vin}\,CO_2$	81.0	0.9	2.6	0.011
$C_{vin}\,ZnCl_2\,CO_2$	84.6	0.8	2.6	0.010
$Pd/C_{cel}\,CO_2$	90.2	1.2	0.4	0.014
$Pd/C_{cel}\,ZnCl_2\,CO_2$	80.5	1.6	1.1	0.020
$Pd/C_{vin}\,CO_2$	81.6	0.9	2.4	0.011
$Pd/C_{vin}\,ZnCl_2\,CO_2$	77.3	0.7	2.5	0.009
$Ru/C_{cel}\,CO_2$	89.1	1.1	0.6	0.012
$Ru/C_{cel}\,ZnCl_2\,CO_2$	81.3	1.5	1.0	0.018
$Ru/C_{vin}\,CO_2$	78.6	1.2	2.7	0.016
$Ru/C_{vin}\,ZnCl_2\,CO_2$	75.0	0.5	2.3	0.007
$Au/C_{cel}\,CO_2$	91.1	1.0	0.4	0.011
$Au/C_{cel}\,ZnCl_2\,CO_2$	88.7	0.4	0.4	0.005
$Au/C_{vin}\,CO_2$	80.8	1.1	2.6	0.015
$Au/C_{vin}\,ZnCl_2\,CO_2$	77.2	0.7	2.4	0.008

The obtained XRD patterns of all solids are illustrated in **Figure 1**.

Although the studied biochars are amorphous, they all can contain some crystalline character, as indicated by three Bragg peaks, the (002), (100) and (110) diffraction peaks (at 2Θ = 24.7, 43.1, and 79.8, respectively) which are indicative of the crystallite orientation, size, and abundance.

The cellulose derived carbons have weaker and just slightly defined diffractions than for vine shoot ones, indicating their higher amorphous character [48]. A small shift in the

diffraction angle of (002) lines is also visible. Moreover, both pretreated chars (C_{cel} $ZnCl_2$ and C_{vin} $ZnCl_2$) showed also a minor shift of the (002) diffraction peak indicating a higher graphitic character compared to the un-treated carbons.

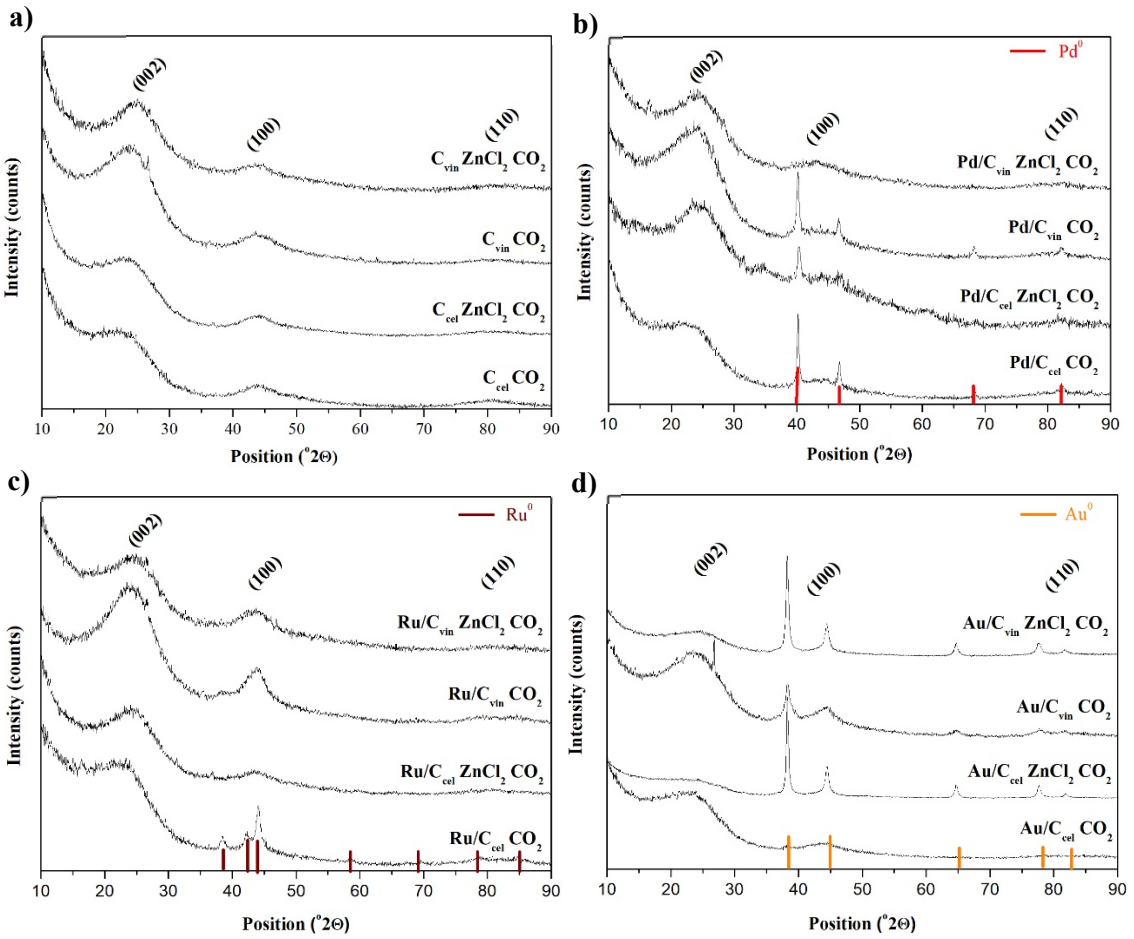

Figure 1. XRD of the samples **a).** Supports, **b).** Palladium, **c).** Ruthenium, **d).** Gold catalysts.

Crystallinity of the biochars were also studied by Raman spectroscopy (**figure S1**, supporting information). Following the criteria of Kouketsu et al. [49], the shape of the first order Raman spectra of all materials is similar to that of medium grade carbonaceous materials, in which up to 5 bands can be observed (called G, D1, D2, D3 and D4, at around 1580, 1350, 1620, 1530 and 1150 cm^{-1}, respectively). These are carbonaceous materials which a medium-to-high amorphousness degree, with a certain transformation to

crystalline graphite as evidenced by the prominent G-band. These authors also suggested that for carbonaceous materials in this range of crystallinity, a suitable criterion for evaluating the crystallinity degree is the G/D1 intensity ratio, which must be <1.5, and increasing with the amorphous character of the solid. In our materials, slightly higher G/D1 intensity ratios were found for cellulose-derived samples than for vine shoot ones (1.062 Ccel CO_2 vs 1.059 Cvin CO_2 and 1.058 Ccel $ZnCl_2$ CO_2 vs 1.045 Cvin $ZnCl_2$ CO_2, respectively), indicating their higher amorphous character in good agreement with the qualitative XRD analysis. In the same way, the G/D1 values of the carbon materials produced after $ZnCl_2$ treatment exhibit a lower G/D1 ratios, indicating a higher crystalline character. Additionally, a small shift of the band D towards higher Raman shifts was found in the vine shoot carbons and in the pretreated samples, indicating a change in the crystallinity of the materials.

In any case, the main conclusion is that all samples show comparable crystallinity, with no significant differences in this structural parameter. A similar conclusion can be extracted from the detailed analysis of the XRD diffractograms, (**Table 2**). R values of vine shoot derived carbons are higher than those of cellulose derived ones, indicating a lower concentration of single carbon layers, meaning higher graphitization. Accordingly, these materials exhibit higher crystallite height (L_c) values indicating lower values of the stacking height between the graphene sheets [48]. At the same time, as demonstrated by Li et al [48], the diffraction angles and FWHMs are strongly influenced by the distortion factors [48]. Evidently, evaluation of the R and L_c values for the prepared catalysts is even more complicated due to possible distortions induced by the presence of nanoparticles. In any case, differences in the lattice parameters of the catalysts with respect to those of the supports are not significant and similar crystallinity of the formed carbon materials can be suggested. In addition to carbon signals, several diffraction peaks

ascribed to the metal phase appear in the diffraction patterns of the reduced catalysts, (**Figure 1b-d)**. Metallic palladium (Cubic, ICDD 00-004-0784, with peaks at 2θ≈ 40.1°, 46.7°, 68.1°, 82.1° and 86.6° due to the {111}, {200}, {220}, {311} and {222} family planes, respectively), Metallic ruthenium (hexagonal, ICDD 00-006-0663, peaks at 2θ≈ 38.4°, 42.2° and 44° of {100}, {002}, and {101} family planes). and metallic gold (Cubic, ICDD 00-004-0784, with peaks at 2θ≈ 38.2°, 44.4°, 64.6°, 77.5° and 81.7° corresponding to the {111}, {200}, {220}, {311} and {222} family planes, respectively) were detected. No peaks ascribed to any other crystalline species were visible, demonstrating the complete reduction of the metallic precursors.

The average metal particle sizes in the catalysts were calculated from the broadening of the {111} diffraction line of the corresponding metal (Pd= 40.2°; Ru=38.4 and Au= 38.2°), applying the Scherrer's equation (**Table 2**). In some catalysts, no metallic diffraction peaks were observed (for instance, most of the ruthenium samples). Since the metallic content in all samples is similar, this can be explained assuming that the average metal particle size is below the XRD detection limit (4-5 nm).

It is clear from the results shown in **Table 2** that not only the carbon support nature, but also the nature and characteristics of the metal and metal precursor as well as the synthesis method determined the final size of the metallic nanoparticles. In general, catalysts prepared by wet impregnation in acetone solutions resulted in smaller particles when using $ZnCl_2$ treated biochars as supports. This must be probably associated with changes in the hydrophobic properties of the carbon surface. In fact, acetone was used instead of water in order to diminish the repulsion between the metallic precursor and the support because of the hydrophobic character of the biochars.

The situation is opposite in the case of gold catalysts, prepared by the colloidal route, where higher gold sizes are obtained over supports obtained from $ZnCl_2$-treated biomass.

Smaller gold nanoparticles were produced on the biochars prepared from cellulose. Besides the use of water as a solvent, the colloidal route implies a transfer of the gold nanoparticles from the colloidal solution to the carbon support surface. Then, the electrostatic interactions are the dominant ones thereby acidity and functionalization of the surface play a major role in the anchoring of the metallic particles. Additionally, $ZnCl_2$ leftovers on the support surface seem to play a negative role in the gold dispersion, probably favoring the surface gold mobility and thus the sintering.

Table 2. Structural parameters calculated from XRD

Sample	Average Particle Size (nm)	L_c Parameter (Å)	R value (002)
$C_{cel}\,CO_2$	-	15	1.6
$C_{cel}\,ZnCl_2\,CO_2$	-	12	1.6
$C_{vin}\,CO_2$	-	13	1.9
$C_{vin}\,ZnCl_2\,CO_2$	-	14	1.7
$Pd/C_{cel}\,CO_2$	37	13	1.5
$Pd/C_{cel}\,ZnCl_2\,CO_2$	22	12	1.5
$Pd/C_{vin}\,CO_2$	32	12	1.9
$Pd/C_{vin}\,ZnCl_2\,CO_2$	N.A.	15	1.7
$Ru/C_{cel}\,CO_2$	12	15	1.7
$Ru/C_{cel}\,ZnCl_2\,CO_2$	N.A.	13	1.7
$Ru/C_{vin}\,CO_2$	N.A.	13	2.3
$Ru/C_{vin}\,ZnCl_2\,CO_2$	N.A.	14	1.7
$Au/C_{cel}\,CO_2$	6	13	1.7
$Au/C_{cel}\,ZnCl_2\,CO_2$	25	13	1.5
$Au/C_{vin}\,CO_2$	8	12	2
$Au/C_{vin}\,ZnCl_2\,CO_2$	21	13	1.8

*NA= Not Available.

The DRIFTS spectra of the obtained biochars supports and catalysts are shown in **Figure 2**.

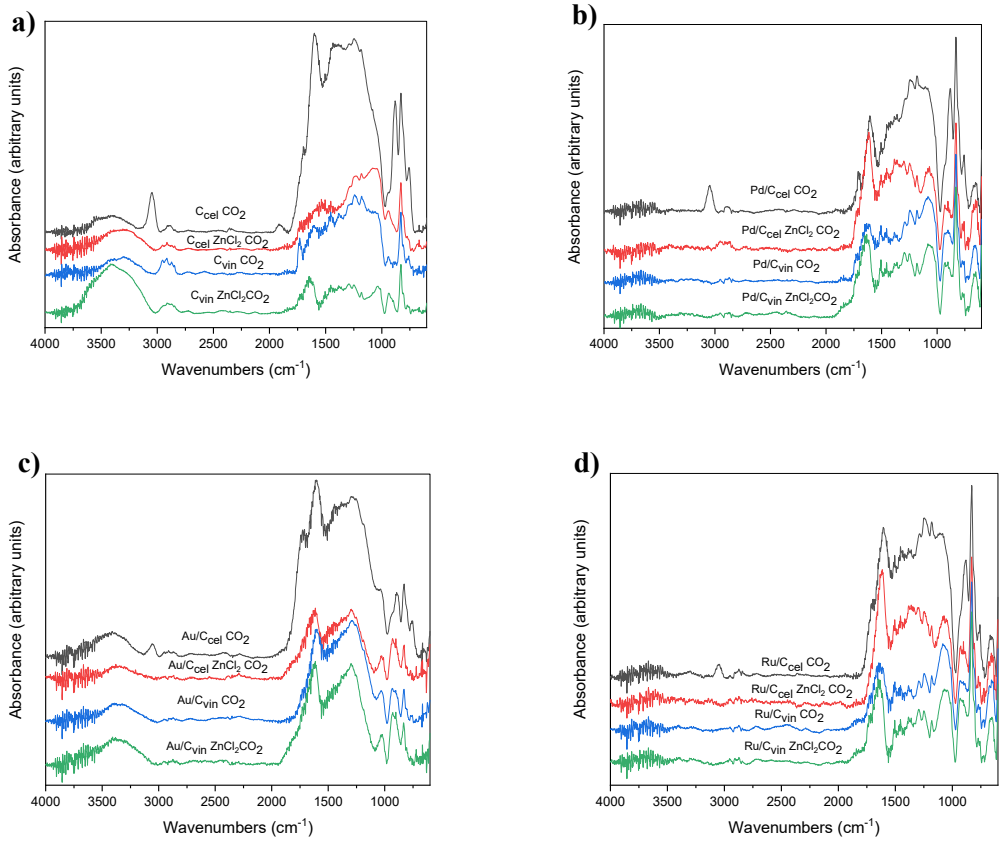

Figure 2. DRIFTS spectra of **a).** biochars and biochars catalysts **b).** palladium **c).** gold and **d).** ruthenium.

All supports exhibit bands characteristic of different functional groups, indicating effective functionalisation of the carbon surfaces. Aromatic and aliphatic hydrocarbons, as well as different oxygenated compounds were detected. All solids show a very broad band (with several components) in the 3700-3200 cm^{-1} region, characteristic of hydrogen-bridged OH stretching of adsorbed water, indicating existence of several species able to adsorb H_2O, probably hydroxyl groups of aliphatic alcohols and/or phenol groups. They also exhibit several bands between 3000 and 2800 cm^{-1} attributed to existence of aliphatic C-H bonds (aliphatic alkyl groups). Presence of C=O groups of different functionalities is also envisaged by the band at 1730 cm^{-1} and others weak ones at 1645, 1695 and 1765 cm^{-1}. The bands in the 1030-1300 cm^{-1} region are characteristics of C-O single bonds

(ethers, alcohols etc.). The bands at ca. 1602 cm^{-1} are due to C=C vibrations while those at ca. 1430 are assigned to aliphatic C-C bonds and/or carboxylate groups [50-52].

Although intense bands at 828 and 775 cm^{-1} demonstrate presence of alkyl-substituted benzenes in all samples (two adjacent (828 cm^{-1}) and three adjacent (775 cm^{-1}) CH groups in individual aromatic nuclei) [53], only in the case of the C_{cel} CO_2 catalyst an intense band at 3047 cm^{-1} due to aromatic C-H groups and a very intense band at 880 cm^{-1} due to isolated CH groups in individual aromatic nuclei were visible pointing out on the existence on the surface of this sample penta or tetra-substituted aromatics [53]. This result is in good agreement with the work of Caturla et al. [43], where activation by HNO_3 or $ZnCl_2$ removed tar formation during the heat treatment leading to more aliphatic carbons. In this sample also a band at 1910 cm^{-1} was detected, which could be attributed to cyclic anhydride or lactone groups [54]. Moreover, intensity of the C=C vibration band at 1602 cm^{-1} increases to a large extent in this carbon.

It is important to note that the presence of oxygenated acid functionalities can play a decisive role during several catalytic reactions, for instance hydrodeoxygenation (HDO) of lignin derived biomass model compounds or the Fischer -Tropsch synthesis [55].

The DRIFTS spectra of the prepared catalysts (**Figure 2 b, c and d**) did not show any significant changes with respect to those of the supports, even if there was a substantial loss of the surface groups. It is interesting to note that impregnation (Pd and Ru) gives carbonaceous materials which decreasing amounts of the surface hydroxyl groups. This is indicative that metal deposition implies interactions between such surface groups of the support with the metal precursors. Thus, these surface functionalities, particularly hydroxyl groups, seems to act as anchoring centers of the metal active phase, favouring higher metal dispersion, better catalyst stability and minimising leaching.

On the contrary, the colloidal route carried out for the deposition of Au, did not alter the concentration of such groups while a strong removal of aromatics and C=O groups from the support surface was observed.

Textural properties of the prepared solids are listed in **Table 3**. In general, the use of CO_2 as pyrolysis atmosphere is a useful strategy to produce micro and mesoporous carbons [11].

CO_2 can be considered as a physical activation agent [56] because it participates in pyrolysis through the reverse Boudouard reaction, eq 1., which decreases the carbon yield and leads to a successive removal of carbon from the pores.

$$C + CO_2 \longleftrightarrow 2\ CO \qquad (1)$$

Biochar from cellulose and vine shoot pyrolized in CO_2 (without $ZnCl_2$ treatment) exhibit type I isotherms, characteristic of microporous materials.

However, double physical and chemical activated biochars showed isotherms of type IV, characteristic of mesoporous materials.

Although many chemical activation treatments have been previously reported in the literature for this type of biomass [12], both physical and chemical activation with CO_2 and zinc chloride has not been extensively studied previously for vine shoot. As shown in **Figure 3**, in line with the literature, biochars derived from CO_2 slow pyrolysis, are mostly microporous materials (approximately 90%), with specific surfaces area below ca. 400 m^2/g [12]. The narrow microporosity of these samples is evidenced by the lack of equilibrium in the measurement of the adsorption isotherms.

However, the physicochemical activation treatment generates a higher specific surface in both biochars (ca. 800 and 1500 m^2/g, respectively) and the microporosity fraction decreased to below ca. 10%.

It was reported [43] that an increase in porosity and surface area after $ZnCl_2$ chemical activation process suggests that such porosity increase could be related to the interstices left by $ZnCl_2$ incorporated in the carbon structure after the exhaustive washing and that $ZnCl_2$ introduced into the particle governs carbon porosity during heat treatment leading to mesoporous materials.

From the distributions of pore sizes **(Figure 3 b and c)**, the mesoporous character of the carbon materials treated with $ZnCl_2$ is evident, corresponding to the pore sizes of ca. 3 nm. As has been recently stated by Brewer et al. [57], precise characterization of the pore structure and pore size distribution of biochar is still challenging, because the pore sizes of biochars usually span a range over at least five orders of magnitude.

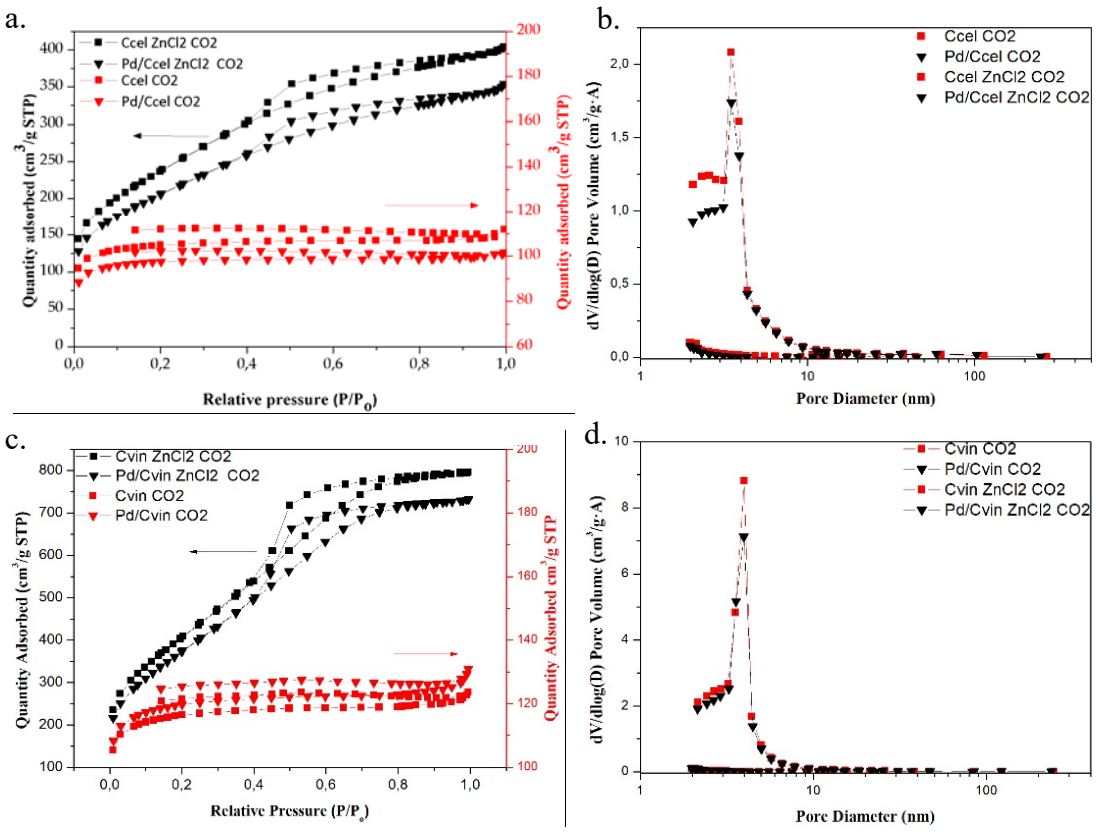

Figure 3. Textural properties of the catalysts.

The textural properties of the catalysts are similar to those of the corresponding supports, indicating that the synthesis method did not influence to a large extent the texture of the solid. The pore size distribution of the starting carbon was preserved, although deposition of the active phase induced a decrease of the total surface area and the pore volume by the partial blockage of the porous structure with the metallic nanoparticles, as reported previously [29].

A slight increase in microporosity was found for all catalysts, which could be related to the effect discussed above.

Table 3. Textural properties of the samples.

Sample	S_{BET} (m^2/g)	Ext. Surface Area (m^2/g)	Microporosity (%)	V_{BHJ} (cm^3/g)	D_{mean} (nm)
$C_{cel}CO_2$	357	49	86	0.022	N.A.
$C_{cel}ZnCl_2CO_2$	794	715	10	0.499	2.9
$C_{vin}CO_2$	371	42	89	0.018	N.A.
$C_{vin}ZnCl_2CO_2$	1479	1479	0	1.390	3.3
$Pd/C_{cel}CO_2$	326	35	89	0.013	N.A.
$Pd/C_{cel}ZnCl_2CO_2$	737	655	11	0.476	2.9
$Pd/C_{vin}CO_2$	401	51	87	0.029	N.A.
$Pd/C_{vin}ZnCl_2CO_2$	1362	1362	0	1.279	3.3
$Ru/C_{cel}CO_2$	185	17	91	0.002	N.A.
$Ru/C_{cel}ZnCl_2CO_2$	763	675	11.5	0.488	2.9
$Ru/C_{vin}CO_2$	326	42	87	0.015	N.A.
$Ru/C_{vin}ZnCl_2CO_2$	1454	1450	0	1.32	3.4
$Au/C_{cel}CO_2$	353	42	88	0.015	N.A.
$Au/C_{cel}ZnCl_2CO_2$	790	702	11.1	0.481	2.8
$Au/C_{vin}CO_2$	317	18	94.3	0.017	N.A.
$Au/C_{vin}ZnCl_2CO_2$	1521	1521	0	1.40	3.2

*NA= Not Available.

The real metal content measured by ICP-MS is summarized in **Table 4**. In all cases, a metal content similar to the nominal one (2 wt.%) was obtained. In the case of gold catalysts, synthesized by the colloidal method, and for the carbon supports prepared from biomass without chemical activation (C_{cel} and C_{vin}), the deposited amount of gold is lower than the nominal value. This could be related with the microporous and hydrophobic character of the material, which induces a poor attachment of the active phase to the surface of the char in aqueous media due to washing, as well known and reported in previous works [29,34]. However, for the catalysts synthesized with the carbon support prepared with physicochemical activation, having a mesoporous character, higher Au loadings were obtained. In some cases, even values higher than the nominal ones were obtained. These results are explained by the observed lixiviation of zinc chloride during gold deposition carried out in aqueous media, **table 5**.

Differences in the gold uptake could be also due to differences in support surface acidity. Changes in the amount and nature of the acidic surface functionalities result in changes in the PZC and IEP values, and also in the hydrophilic character of the carbon. In this sense, by comparing the gold uptake (Table 4) and IEP values (Figure 7) it is clear that for the CO_2-activated carbons, a lower gold uptake (0.13% vs 0.57%) is obtained for the sample with a lower IEP (5.5 vs 6.3).

Figure 4 displays representative TEM micrographs and metal particle size distribution for the prepared catalysts. A good correlation was achieved between the average metal particle size determined by TEM and that obtained by XRD using the Scherrer's equation (**Table 6**). However, a higher discrepancy was obtained for Pd catalysts.

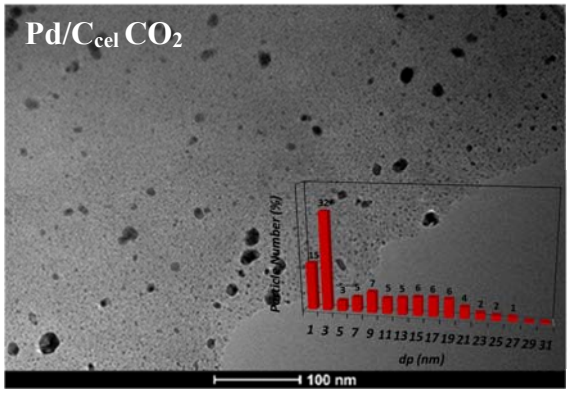
Pd/Ccel CO2
Particle Number (%)
dp (nm)
100 nm

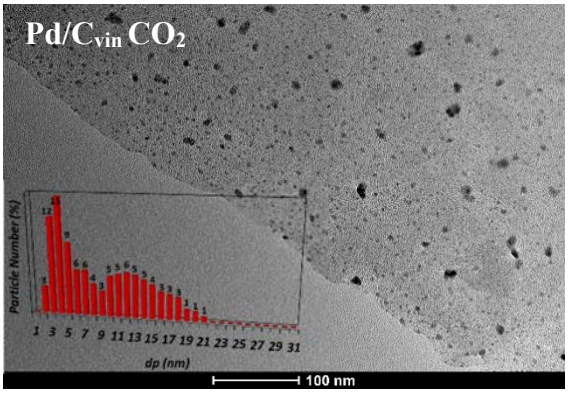
Pd/Cvin CO2
Particle Number (%)
dp (nm)
100 nm

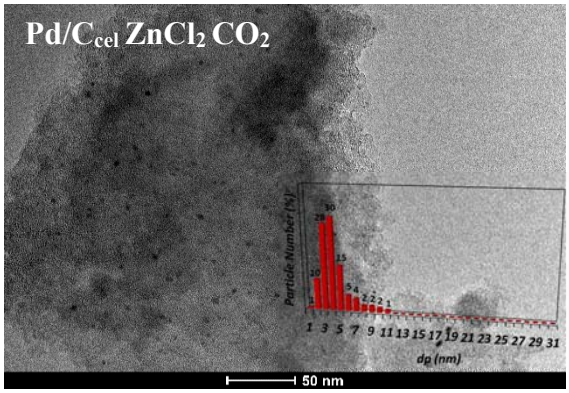
Pd/Ccel ZnCl2 CO2
Particle Number (%)
dp (nm)
50 nm

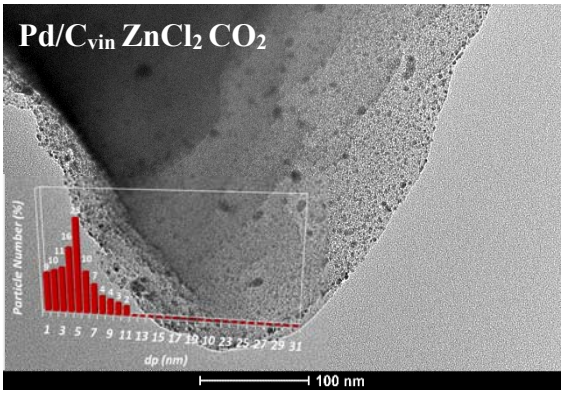
Pd/Cvin ZnCl2 CO2
Particle Number (%)
dp (nm)
100 nm

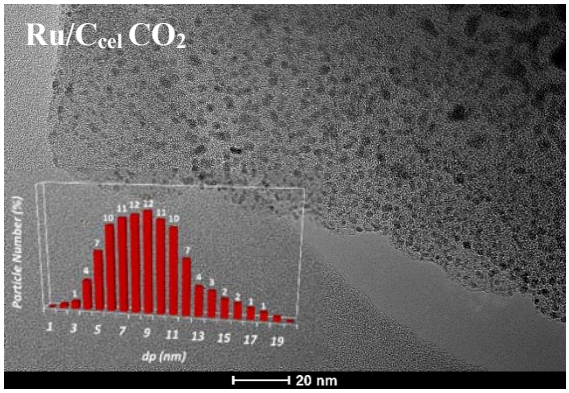
Ru/Ccel CO2
Particle Number (%)
dp (nm)
20 nm

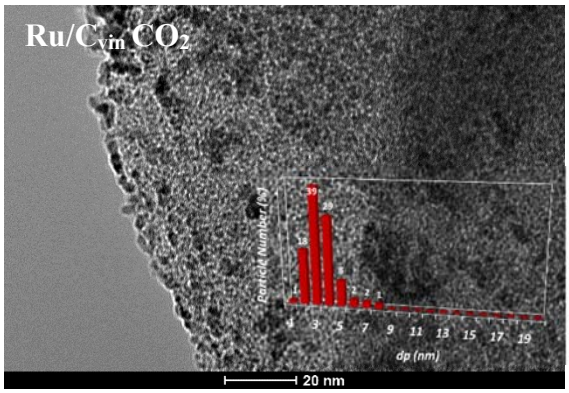
Ru/Cvin CO2
Particle Number (%)
dp (nm)
20 nm

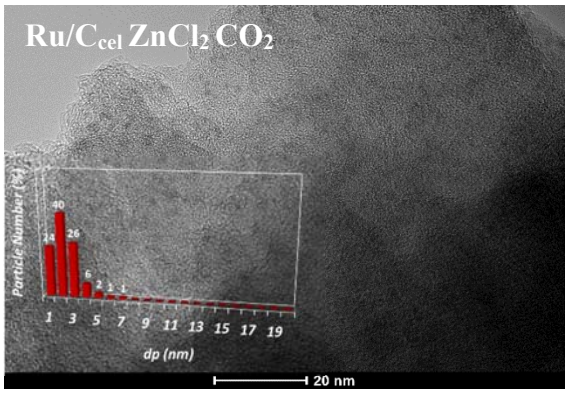
Ru/Ccel ZnCl2 CO2
Particle Number (%)
dp (nm)
20 nm

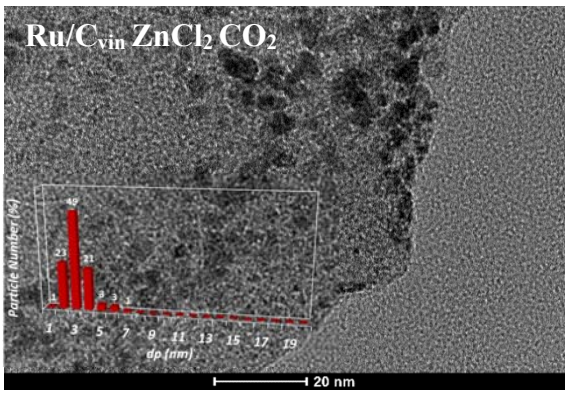
Ru/Cvin ZnCl2 CO2
Particle Number (%)
dp (nm)
20 nm

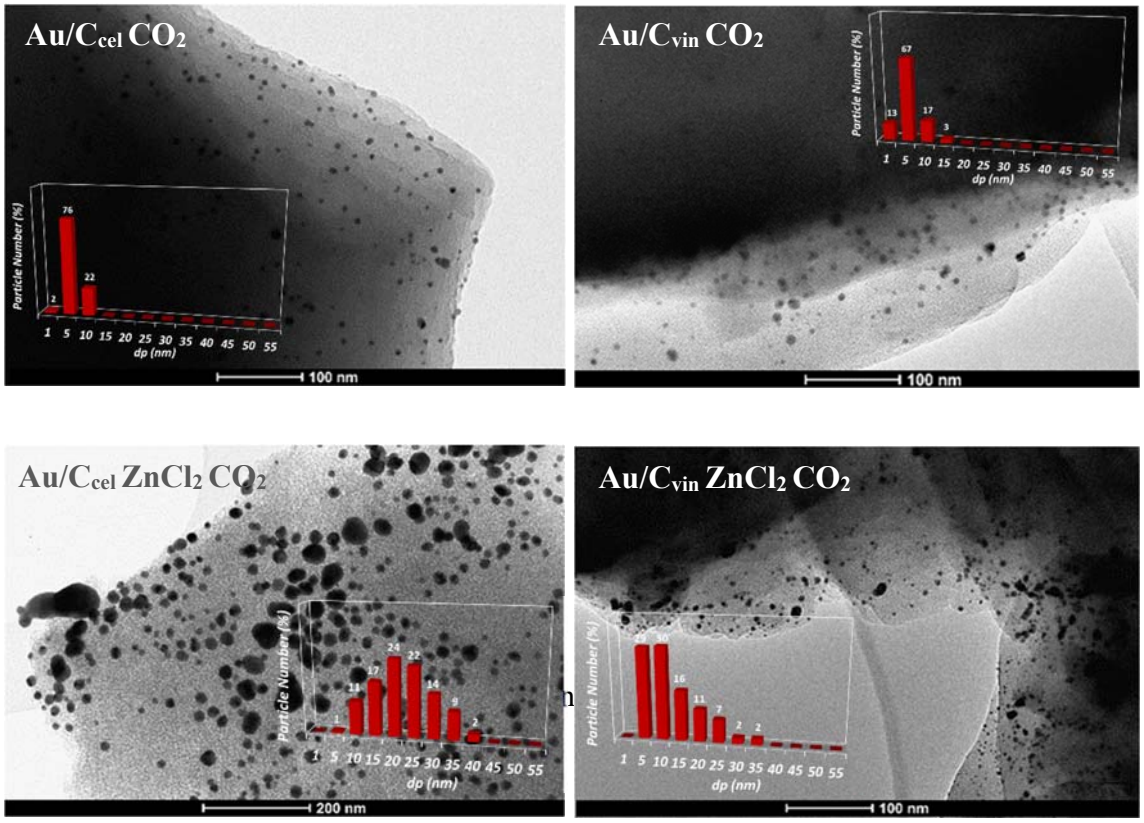

Table 4. Mean particle size, metal loadings and dispersion.

Sample	% Metal [ICP]	Average particle size (TEM, nm)	Average particle size (XRD, nm)	Calculated dispersion (TEM, %)
Pd/C_{cel} CO_2	1.66	19	37	8
Pd/C_{cel} $ZnCl_2$ CO_2	2.56	6	22	22.2
Pd/C_{vin} CO_2	1.78	13.8	35	11
Pd/C_{vin} $ZnCl_2$ CO_2	2.36	6.9	N.A.	19.6
Ru/C_{cel} CO_2	1.08	9.6	12	14.9
Ru/C_{cel} $ZnCl_2CO_2$	2.57	2.7	N.A.	46.7
Ru/C_{vin} CO_2	1.93	3.9	N.A.	33.5
Ru/C_{vin} $ZnCl_2$ CO_2	2.37	3.6	N.A.	36.1
Au/C_{cel} CO_2	0.13	8.4	6	16.6
Au/C_{cel} $ZnCl_2$ CO_2	3.07	24.7	25	6
Au/C_{vin} CO_2	0.57	8.7	8	17.9
Au/C_{vin} $ZnCl_2$ CO_2	1.78	20.9	21	7.8

A monomodal distribution was found for all catalysts except palladium catalysts supported on unpretreated biochars, displaying a bimodal one. This reflects a good adaptability of each synthesis method on the different carbonaceous supports.

With respect to gold catalysts, a wider distribution was found for the catalysts generated on pretreated biochars, suggesting some sintering process of the active phase. According to observations of Oh et al. [58], chlorine can induce a poisoning effect related to the formation of Au-Cl bridges. These Au-Cl species have a higher surface mobility favoring the gold sintering during calcination [59].

Dispersion of the active phase was also calculated from the average metal particle size determined by TEM, the metal content measured by ICP and a mathematical model for cuboctahedral particles [60].

HRTEM micrographs (**Figure S2**), are in good agreement with the TEM distribution particle size and exhibits the characteristics structure of turbostratic biochar, being the dark features the metallic particles. Pd/C_{vin} $ZnCl_2$ CO_2 is shown as a representative example of the Pd catalysts, displaying a discrete lattice-fringe of the face centered cubic (fcc) Pd crystal with a d-spacing of 0.224 nm, which is in agreement with the lattice spacing of the Pd (111) plane reported in the literature [61,62]. In Au/C_{vin} $ZnCl_2$ CO_2 sample, the lattice spacing of the (111) and (200) planes of cubic, ICDD 00-004-0784, gold (0.2355 and 0.203 nm, respectively) are discernible [63]. Finally, ruthenium catalysts exhibit semi-spherical nanoparticles of 5-7 nm in size, in which the interplanar distances of 0.20 and 0.23 nm, corresponding respectively to (101) and (100) planes of metallic Ru (hcp) phase (hexagonal, ICDD 00-006-0663), are distinguishable [64].

STEM micrographs of mesoporous biochars from vine shoot catalysts were analysed (**Figure S3**). STEM images are of high contrast because of the low crystallinity of

biochars and bright dots due to semi-spherical metal particles are visible. High-resolution HAADF-STEM imaging was successfully employed to analyse the dispersion as well as the geometrical and structural characteristics of the metal nanoparticles as a function of the synthesis method. Using the classical impregnation method, most of the pores remain generally filled, while small metallic nanoparticles were well distributed within the pore walls; large metal nanoparticle size are also present close to the external surfaces of the grains. According to the previous discussion and Zhao et al. [65], HAADF images of gold samples prepared by the colloidal method and using the $ZnCl_2$ treated biomass evidence the existence of bigger metallic particles (10–26 nm).

As follows from HRTEM characterization, the ratio of distorted particles increased with a decrease in the particle size. Smaller particles tend to be in a distorted shape because of stronger interactions with the support. According to [66], these distorted particles are of oval shape, therefore, there is a larger interface between the metal and the carbon support than for the spherical particles. Considering these two facts, catalysts with smaller metallic particles have higher metallic exposed surfaces and a higher metal-carbon contact perimeter, which presumably leads to a higher reactivity.

Finally, elemental mapping within a randomly selected area of the catalysts is shown in **Figure S4**. The results agree with other microscopies. The catalysts prepared by the impregnation method (Pd and Ru) show a homogenous distribution of well dispersed metallic particles on the biochar surface. This could be related with the deposition of the metal particles in the mesoporous structure, leading to the observed decrease in the surface area of the support. Gold catalysts prepared from the colloidal method showed a wider distribution and larger metal particle size on the carbon surface. Moreover, gold and oxygen signals display uniformly, suggesting a close contact between gold and oxygen atoms.

The microstructure of biochars catalysts was studied by SEM (**Figure 5)**. The vine shoot biochars show a porous structure clearly visible and similar to that reported by Valente Nabais et al. [67]. Chemical activated biochar samples display a similar well-developed pore system with however, presence of some residues (**Table 5**) and amorphous carbon formed during carbonization, blocking partially the surface.

According to Reinoso et al. [68] chemical activation with $ZnCl_2$ generates carbonaceous materials with narrower pore size distributions than those obtained by using other chemical activation agents. Additionally, such treatment generates cracks, as illustrated in **Figure 5**, which can easily lead to rupture of the grains.

Nevertheless, in all materials, the organized and regular structure of the biochar is clearly visible by SEM.

In good agreement with other characterization results, the surface morphology of the samples was similar to corresponding support (not shown), suggesting no modifications during deposition of the active phase. SEM micrographs also confirm the heterogeneous metal distribution for palladium and gold catalysts, and more homogeneous one for the ruthenium catalysts.

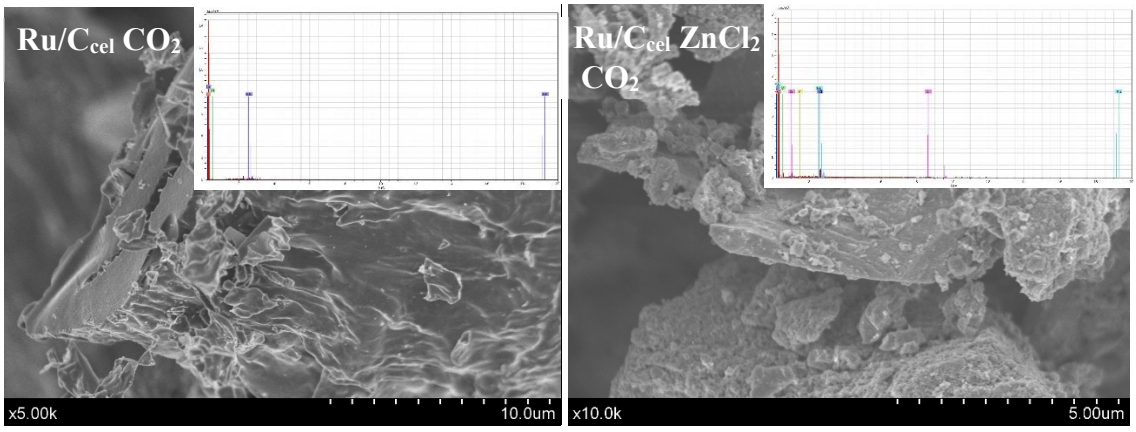

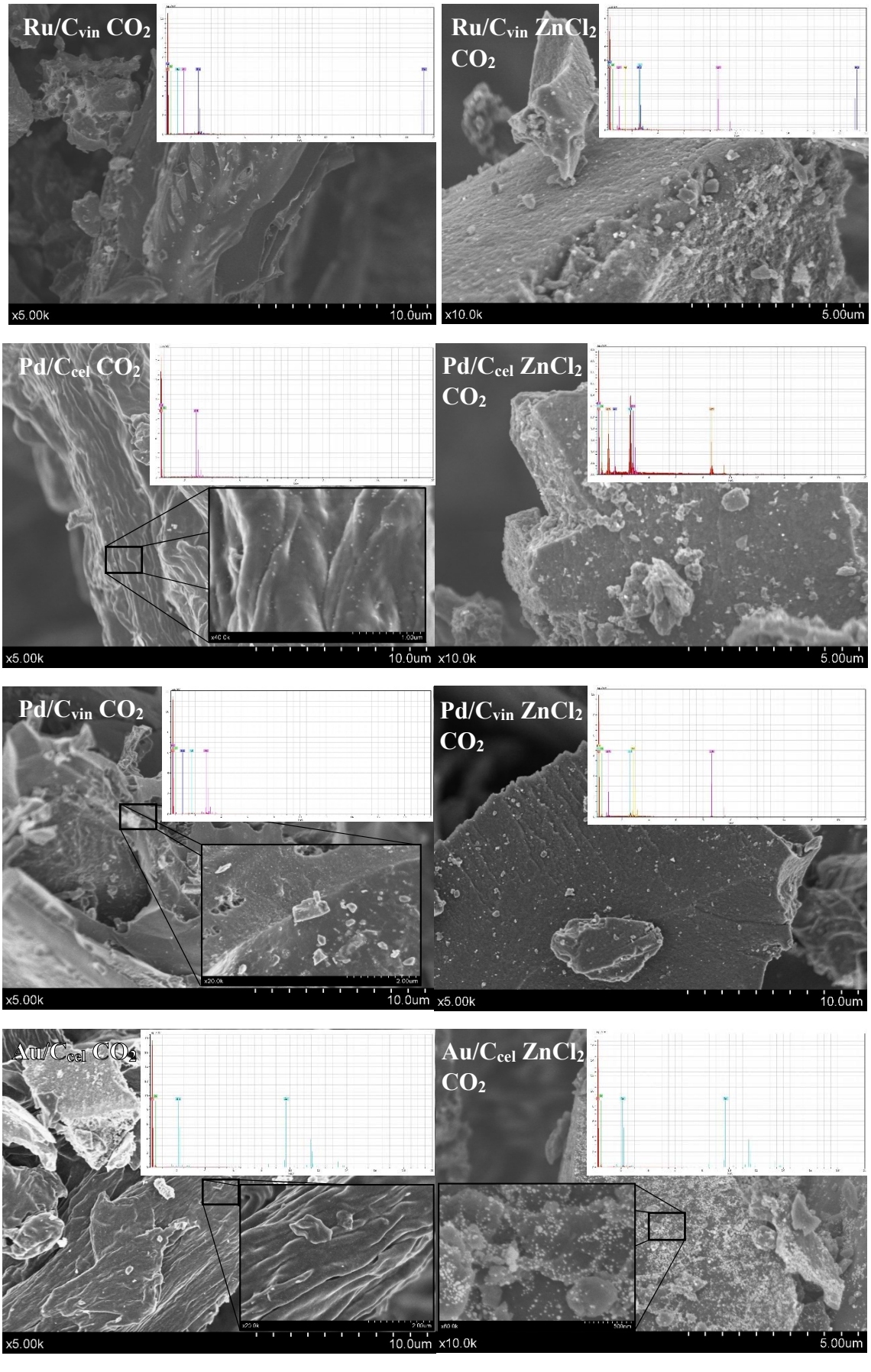
Ru/Cvin CO2
x5.00k
10.0um
Ru/Cvin ZnCl2 CO2
x10.0k
5.00um
Pd/Ccel CO2
x5.00k
10.0um
Pd/Ccel ZnCl2 CO2
x10.0k
5.00um
Pd/Cvin CO2
x5.00k
10.0um
Pd/Cvin ZnCl2 CO2
x5.00k
10.0um
Au/Ccel CO2
x5.00k
10.0um
Au/Ccel ZnCl2 CO2
x10.0k
5.00um

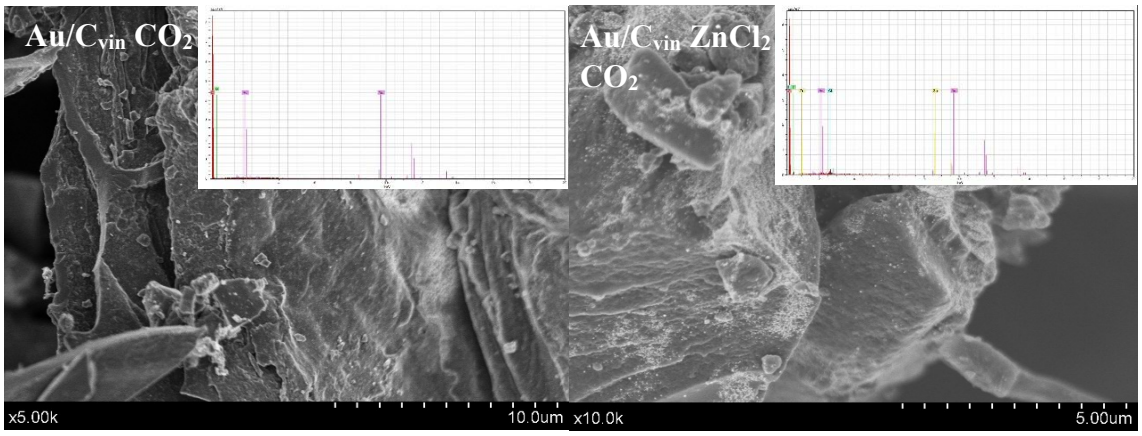

Figure 5. Representative SEM micrographs of the samples.

Semi-quantitative energy disperse X Ray Spectroscopy (EDS) results obtained for all catalysts are closer to the nominal values. It was not possible to quantify the palladium loading. Considering large errors in quantifying very light elements, still the same trends as obtained by ICP were observed. Nevertheless, closer values of the weight percentage for carbon were found being in line with the elemental analysis. The semi quantitative oxygen content values (**Table 7**), indicate a higher functionalization degree in the carbonaceous materials obtained from vine shoot, which could be related with the HNO_3 treatment carried out and the presence of mineral elements.

Table 5. Semi-quantitative energy disperse X Ray Spectroscopy (EDS) results.

Sample	**Carbon [norm. wt.%]**	**Oxygen [norm. wt.%]**	**Noble Metal [norm. wt.%]**	**Chlorine [norm. wt.%]**	**Zinc [norm. wt.%]**
Ru/C$_{cel}$	88.7	8.6	2.7	-	-
Ru/C$_{vin}$	86.2	11.1	2.7	-	-
Ru/C$_{cel}$ ZnCl$_2$	78.5	13.3	1.9	3.1	3.2
Ru/C$_{vin}$ ZnCl$_2$	80.1	11.4	1.3	3.6	3.6
Au/C$_{cel}$	89.4	10.3	0.3	-	-
Au/C$_{vin}$	86.5	12.2	1.4	-	-
Au/C$_{cel}$ ZnCl$_2$	84	10.2	5.1	0.4	0.3
Au/C$_{vin}$ ZnCl$_2$	73.9	17.1	6.8	1.4	0.8

In the case of palladium catalysts, with an apparent discrepancy between XRD and TEM results, a more detailed SEM study reveals the existence of islands enriched in palladium

(**Figure S5**) for the catalysts synthesized onto microporous biochars. This led to larger particle sizes (29 and 21 nm for cellulose and vine shoot derived chars, respectively) and a broader distribution in the particle size histograms for these catalysts, which are in good correlation with the bimodal distribution of particles evidenced by TEM.

This phenomenon was not found for the catalysts supported onto mesoporous biochars, where the average particle size was slightly lower, providing an explanation for the discrepancy between the average particle size measured by TEM and XRD for these samples.

The isoelectric point (IEP) of the prepared solids is presented in **Figure 6**. The values depend on the starting biomass and the preparation conditions and range from 4.3 to 6.3. The results are in good agreement with the literature data for carbons obtained by slow pyrolysis [69]. Low values of pH suggest a proper activation of the carbon surface, with the existence of oxygen-containing functional groups, generally of acidic character, which were detected by DRIFTS **(Figure 2).** According to the DRIFTS observed trend of biochars surface functionalization, it would be expected that biochars from cellulose had lower IEP values than those from the vine shoots, as observed experimentally. In addition, the effect of the joint physicochemical activation could lead to surface activation and subsequently a slight decrease in pH on the surface.

After metal impregnation, in agreement with the literature [29] and our DRIFTS results, a portion of the functionalized surface species was lost, which drives to slightly more alkaline pH values.

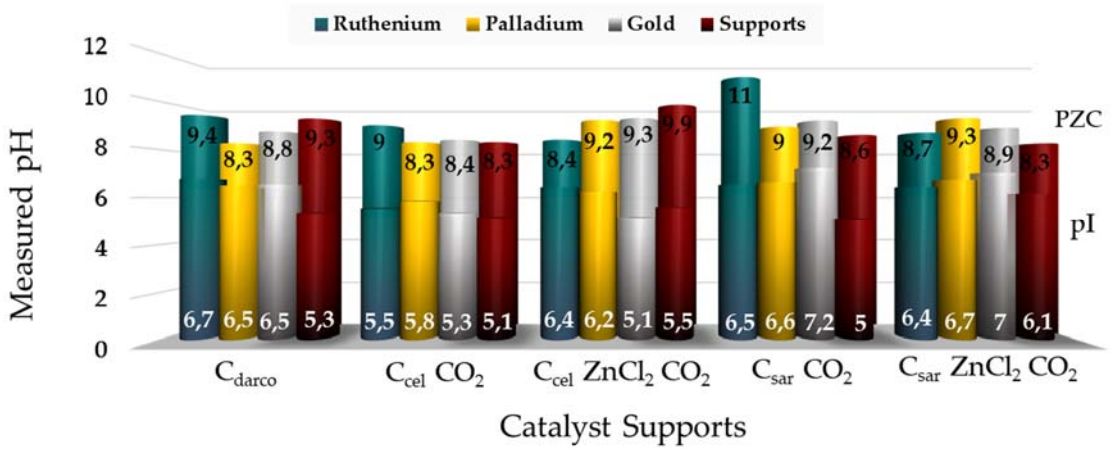

Figure 6. a). Isoelectric point (IEP), **b).** Point zero charge (PZC) of the catalyst and supports.

The value of IEP and PZC of the simple oxides and other common materials are usually similar. It is well known [69], that the isoelectric point (IEP) values are only representative of the external surface charges of carbon particles in solution, whereas the point of zero charge (PZC) varies in response to the net total (external and internal) surface charge of the particles [69-71]. The difference between the value of PZC and IEP represent the degree of uniformity/heterogeneity of total charge distribution of a whole porous particle.

The net PZC curves for all catalysts are shown in **Figure 7,** and the estimated PZC value are reported in **Figure 6b**.

The pH of the surface of biochars prepared from different types of biomass reported by Tan et al. [72], was always higher than 7. Thus, biochars are considered as alkaline solids. As proposed by Lehmann [73], the PZC of biochar is related to the ash content, in such a way that higher the ash content higher the PZC. In our case, as biochars prepared from microcrystalline cellulose are ash-free carbons, they show a pH slightly more acidic than those prepared from the vine shoot.

In general, also the treatment with $ZnCl_2$ results in carbon materials with a lower pH (higher acidity) which is also an evidence of a higher functionalization of the carbon surface, as demonstrated by DRIFTS, as well as a higher oxygen content, since functionalization implies formation of surface oxygenated compounds with acidic groups. As shown in **Figure 7**, all catalysts exhibit a more basic character than the corresponding support, suggesting that in all cases, the metal deposition results in a more basic character of the material. This, as said above, is another evidence of the participation of the acidic surface groups of the support in the noble metal particles anchoring.

Somewhat differently from titration data described in the previous section, all catalysts exhibited a basic character in the surface.

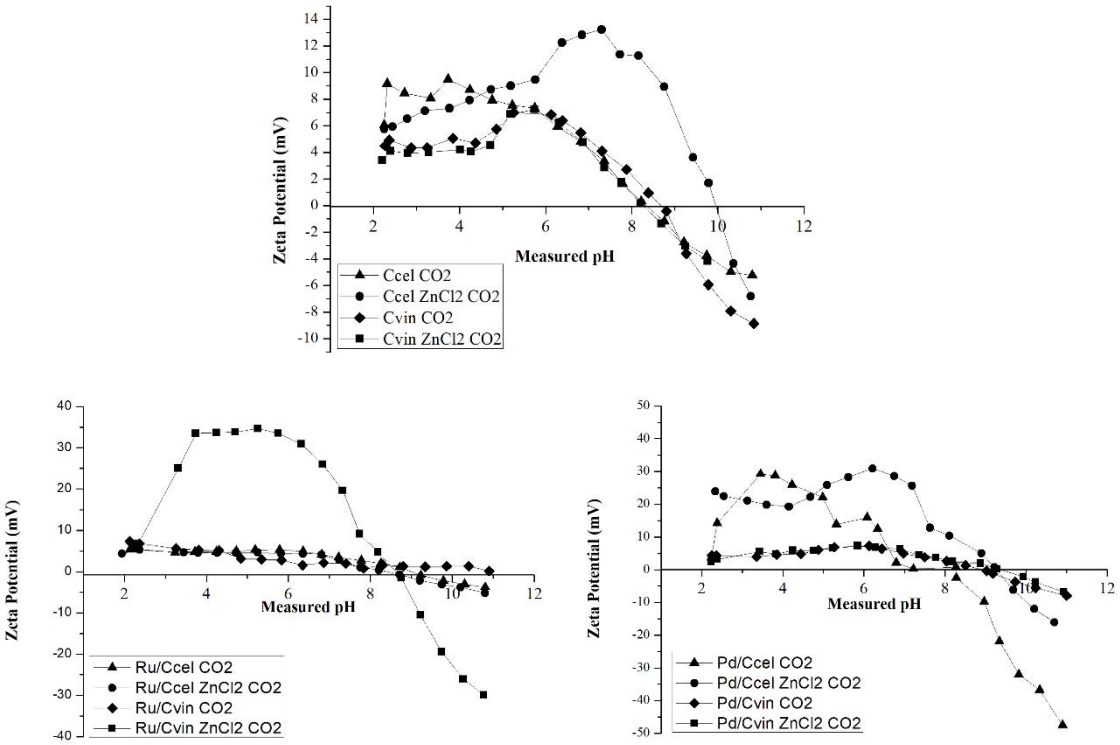

Figure 7. Zeta potential of the catalyst samples and the support.

3. Conclusions

Carbonisation of vine shoot residual biomass and microcrystalline cellulose, as models of lignocellulosic biomass materials, can generate biochars suitable to be used for catalytic purposes.

Textural properties and surface functionality of the prepared biochars can be finely modified via various physical (CO_2) and/or chemical ($ZnCl_2$) treatments. Joint activation results in biochars with significantly developed mesoporosity, BET surface area increasing from 400 to 1060 $m^2 \cdot g^{-1}$, and higher surface acidity, making these materials promising catalyst supports.

Different carbon supported catalysts (containing Pd, Au and Ru) were synthesized by incipient wetness impregnation methods for palladium and ruthenium and a colloidal route for gold. Physicochemical properties of the generated catalysts (e.g., surface area and functionality, porosity, and acidity) are strongly dependent on the origin of biomass and the pre/post treatments. Metallic nanoparticles were successfully deposited on the carbonaceous supports. The presence of oxygenated surface functionalities on the support surface increases the surface acidity and favors deposition of the metal.

In general, this study highlights the benefits of the conventional method of synthesis by impregnation, for the production of biochars supported nanocatalysts containing ruthenium and palladium. However, the preparation of gold catalyst supported on biochars requires other methods of metal deposition, such as the colloidal one. With this methodology, gold uptake and average metallic gold size depend on the surface chemistry of the support, with surface acidity being rather important. Presence of $ZnCl_2$ has a negative effect on the gold particle size.

In both cases, impregnation or colloidal synthesis, the homogeneity and metal particle size and distribution over the carbon support depends on the nature and surface properties of the biochars. The prepared materials represent a set of nanometal (Pd, Au and Ru) catalysts supported on biochars of different textural and surface properties, produced from representative biomass sources, which can serve as a model to study the influence of the active phase and carbon support nature, in the catalytic properties of the metal/carbon materials in several catalytic reactions relevant to refineries, which will be a subject of the part II of this study.

Acknowledgments

Financial support for this work has been obtained from the Spanish Ministerio de Economía y Competitividad (MINECO) (Grants ENE2013-47880-C3-2-R, ENE2017-82451-C3-3-R and ENE2017-82451-C3-1-R) co-financed by FEDER funds from the European Union. J.L. Santos also acknowledges the MINECO for his predoctoral fellowship (BES-2014-068244) and the mobility fellowship (EEBB-I-17-11979).

References

[1] A. Demirbas, Energy Convers. Manage.42 (2001) 1357–1378.

[2] J. Lehmann, Front. Ecol. Environ. 5 (2007) 381–387.

[3] S. Du, J. A. Valla and G. M. Bollas, Green Chem. 15 (2013) 3214–3229.

[4] A. G. W. Bradbury and F. Shafizadeh, Carbon 18 (1980) 109.

[5] W. F. Degroot, T. H. Osterheld and G. N. Richards, Carbon 29 (1991) 185-195.

[6] F. Shafizadeh, J. Anal. Appl. Pyrolysis 3. (1982) 283.

[7] A. M. Dehkhoda, A. H. West and N. Ellis. Appl. Catal. A: Gen. 382 (2010) 197–204.

[8] J.R. Kastner, J. Miller, D.P. Geller, J. Locklin, L.H. Keith and T. Johnson. Catal Today 190 (2012) 122–132.

[9] M. Li, Y. Zheng, Y. Chen and X. Zhu. Bioresour Technol. 154 (2014) 345–348.

[10] S. Li, Z. Gu, B.E. Bjornson and A. Muthukumarappan. J Environ Chem Eng. 1 (2013) 1174–1181.

[11] M. Azuara, E. Sáiz, J. A. Manso, F. J. García-Ramos and J. J. Manyà. J.Anal. Appl.Pyrol. 124 (2017) 719–725.

[12] J. J. Manyà, B. González, M. Azuara and G. Arner, Chem. Eng. J. 345 (2018) 631–639.

[13] J. J. Manyà, M. A. Ortigosa, S. Laguarta and J. A. Manso. Fuel 133 (2014) 163–172.

[14] J. S. Cha, S. H. Park, S. C. Jung, C. Ryu, J. K. Jeon, M. C. Shin and Y. K. Park, J. Ind. Eng. Chem. 40 (2016) 1–15.

[15] J. Marousek, M. Vochozka, J. Plachy and J. Zak, Clean Technol. Environ. Policy 19 (2017) 311–317.

[16] S. Prapagdee, S. Piyatiratitivorakul and A. Petsom, Asian J. Water, Environ. Pollut. 13 (2016) 27–34.

[17] J. D. Lopez-Gonzalez, F. Martinez-Vilchez, and F. Rodriguez-Reinoso. Carbon 18 (1980) 413.

[18] X. H. Lu, J. He, R. Jing, P. P. Tao, R. F. Nie, D. Zhou and Q. H. Xia, Sci. Rep. 7 (2017) 2676.

[19] M. Uchimiya, J. J. Pignatello, J. C. White, S. L. Hu and P. J. Ferreira, Sci. Rep. 7 (2017) 5027.

[20] J. Lee, K. H. Kim and E. E. Kwon, Renew. Sust. Ener. Rev. 77 (2017) 70–79.

[21] W. J. Liu, H. Jiang and H. Q. Yu. Chem. Rev. 115 (2015) 12251–12285.

[22] Q. Wei, H. Fan, F. Qin, Q. Ma and W. Shen. Carbon 133 (2018) 6-13.

[23] S. Teja Neeli, H. Ramsurn. Carbon 134 (2018) 480-490.

[24] M. Inagaki, M. Toyoda, Y. Soneda, S. Tsujimura and T. Morishita. Carbon 107 (2016) 448-473.

[25] K. Weber, P. Quicker, Fuel 217 (2018) 240-261.

[26] Z. Zhu, H. Tan, J. Wang, S. Yu and K. Zhou, Green Chem. 16 (2014) 2636–2643.

[27] H. Lee, H. Kim, M. J. Yu, C. H. Ko, J. K. Jeon, J. Jae, S. H. Park, S. C. Jung and Y. K. Park. Sci. Rep. 6 (2016) 28765.

[28] C. Newman, X. Zhou, B. Goundie, I. T. Ghampson, R. A. Pollock, Z. Ross, M. C. Wheeler, R. W. Meulenberg, R. N. Austin and B. G. Frederick, Appl. Catal. A: Gen. 477 (2014) 64–74.

[29] J.L. Santos, M. Alda-Onggar‧, V. Fedorov‧, M. Peurla‧, K. Eränen‧, P. Mäki-Arvela‧, M.Á. Centeno‧ and D. Yu. Murzin. Appl. Catal. A: Gen. 561 (2018) 137-149.

[30] R. Nie, H. Yang, Y.H. Zhang, X. Yu and X. Zhou, Q. Zia, Green Chem. 19 (2017) 3126–3134.

[31] G. Neri, M.G. Musolino, C. Milone, A.M. Visco and A. Di Mario, J. Mol. Catal. A: Chem. 95 (1995) 235–260.

[32] I. Yati, A.A. Dwiatmoko, J.S. Yoon, J.-W. Choi, D. Jin Suh, J. Jae and J.-M. Ha, Appl. Catal. A: Gen. 524 (2016) 243–250.

[33] G.C. Torres, E.L. Jablonski, G.T. Baronetti, A.A. Castro, S.R. De Miguel, O.A. Scelza, M.D. Blanco, M.A. Pena-Jimenez and J.L.G. Fierro. Appl. Catal. A: Gen. 161 (1997) 213–260.

[34] C. Megías-Sayago, J.L. Santos, F. Ammari, M. Chenouf, S. Ivanova, M.A. Centeno and J.A. Odriozola. Catal. Today 306 (2018) 183–190.

[35] C.H. Bartholomew, R.J. Farrauto, Fundamentals of Industrial Catalytic Processes, second ed., Wiley-Interscience, Hoboken, USA, 2006.

[36] D. Lozano-Castello, J.M. Calo, D. Cazorla-Amorós and A. Linares-Solano. Carbon 45 (2007) 2529-2536.

[37] Y. Guo, D. A. Rockstraw. Carbon 44 (2006) 1464-1475.

[38] M. Haruta, N. Yamada, T. Kobayashi and S.J. Iijima, J. Catal. 115 (1989) 301

[39] J. Luo, W. Chu, S. Sall and C. Petit, Colloids Surf. A Physicochem. Eng. Asp. 425(2013) 83.

[40] Q. Li, Q. Tao, C. Yuan, Y. Zheng, G. Zhang and J. Liu, Int. J.Heat Mass Transf. 120 (2018) 1162-1172.

[41] H. Takagi, K. Maruyama, N. Yoshizawa, Y. Yamada and Y. Sato, Fuel 83 (2004) 2427–2433.

[42] H. Markus, P. Mäki-Arvela, N. Kumar, N.V. Kulkova, P. Eklund, R. Sjöholm, B. Holmbom, T. Salmi and D. Yu Murzin, Catal. Lett. 103 (2005) 1-2.

[43] F. Caturla, M. Molina-Sabio, and F. Rodriguez Reinoso. Carbon 29 (1991) 999-1007.

[44] I.Y. Eom, JY. Kim, TS. Kim, SM. Lee, D. Choi, IG. Choi,J.-W. Choi. Bioresour Technol 104 (2012) 687-698.

[45]. GN. Richards, GC. Zheng. J Anal Appl Pyrol 21 (1991) 133-147.

[46] F. Shafizadeh and Y. Sekiguchi, Carbon 21 (1983) 511-516.

[47] S.A. Visser, Environ. Sci. Technol. 17 (1983) 412–417.

[48] Z. Q. Li, C. J. Lu, Z. P. Xia, Y. Zhou and Z. Luo. Carbon 45 (2007) 1686–1695.

[49] Y. Kouketsu, T. Mizukami, H. Mori, S. Endo, M. Aoya, H. Hara, D. Nakamura and S. Wallis, Island Arc 23 (2014) 33-50.

[50] N. Iwashita, C.R. Park, H. Fujimoto, M. Shiraishi and M. Inagaki, Carbon 42 (2004) 701–714.

[51] U. Zielke, K.J. Huttinger and W.P. Hoffman, Carbon 34 (1996) 983-998

[52] B.J. Meldrum, C.H. Rochester, Fuel 70 (1991) 57-63.

[53] B. J. Meldrum, C.H. Rochester, J. Chem. Soc. Faraday Trans. 86 (1990) 861-865.

[54] P.E. Fanning, M.A. Vannice. Carbon 31 (1993) 721-730.

[55]. G. T. Kasun Kalhara Gunasooriya, A. P. van Bavel, H. P. C. E. Kuipers and M. Saeys, ACS Catal. 6 (2016) 3660−3664.

[56] G. Pilon, J.M. Lavoie. ACS Sustain. Chem. Eng. 1 (2013) 198–204.

[57] C.E. Brewer, V.J. Chuang, C.A. Masiello, H. Gonnermann, X. Gao, B. Dugan, L. E. Driver, P. Panzacchi, K. Zygourakis and C.A. Davies. Biomass Bioenergy 66 (2014) 176–185.

[58] H.S. Oh, J.H. Yang, C.K. Costello, Y.M. Yang, S.R. Bare, H.H. Kung and M.C. Kung, J. Catal. 210 (2002) 375.

[59] S. Ivanova, C. Petit, V. Pitchon, Applied Catalysis A: General 267 (2004) 191–201.

[60] Y.F. Han, Z. Zhong, K. Ramesh, F. Chen, L. Chen, J. Phys. Chem. C 111 (2007) 3163–3170.

[61] X. Wang, G.W. Qi, C.H. Tan, Y.P. Li, J. Guo, X.J. Pang and S.Y. Zhang. Int. J. Hydr. Ener. 39 (2014) 837–843.

[62] F. Sanchez, D. Motta, L. Bocelli, S. Albonetti, A. Roldan, C. Hammond, A. Villa and N. Dimitratos. J. Carbon Res.4 (2018) 26.

[63] T. Shimizu, T. Teranishi, S. Hasegawa and M. Miyake. J. Phys. Chem. B 107 (2003) 2719 -2724.

[64] G. Viau, R. Brayner, L. Poul, N. Chakroune, E. Lakaze, F. Fièvet-Vincent and F. Fièvet. Chem. Mater. 15 (2003) 486.

[65] J. Zhao, B. Wang, X. Xu, Y. Yu, S. Di, H. Xu, Y. Zhai, H. He, L. Guo, Z. Pan and X. Li. J. Catal. 350 (2017) 149–158.

[66] M. Girleanu, S. Lopes Silva, D. Ihiawakrim, A. Chaumonnot, A. Bonduelle-Skrzypczak, F. Lefebvre, V. Dufaud, A. S. Gay and O. Ersen. Microp. Mesop.Mater. 217 (2015) 190-195.

[67] J.M. Valente Nabais, C. Laginhas, P.J.M. Carrott and M.M.L. Ribeiro Carrott. J. Anal. Appl. Pyrolysis 87 (2010) 8–13.

[68] M. J. Prauchner, F. Rodríguez-Reinoso. Microp. Mesop.Mater. 152 (2012) 163–171.

[69] J.A. Menéndez, M.J. Illán-Gómez, C.A. Leon y Leon and L.R. Radovic. Carbon 33, (1995) 1655-1659.

[70] M. O. Corapcioglu and C. P. Huang. Carbon 25 (1987) 569-5781.

[71] G. Newcombe, R. Hayes and M. Drikas. Colloids Surf. A 78 (1993) 65.

[72] Z. Tan, C. S.K. Lin, X. Ji and T. J. Rainey. Appl. Soil Ecol. 116 (2017) 1–11.

[73] J. Lehmann, Front. Ecol. Environ. 5 (2007) 381–387.